The Seismic Record
A journal of the Seismological Society of America

The 28 March 2025 M_w 7.8 Myanmar Earthquake: Preliminary Analysis of an ~480 km Long Intermittent Supershear Rupture

Lingling Ye*[1], Thorne Lay[2], and Hiroo Kanamori[3]

Abstract

On 28 March 2025, an M_w 7.8 shallow strike-slip earthquake ruptured ~480 km of the 1200 km long Sagaing fault extending north–south across central Myanmar. This active right-lateral fault hosted six major earthquakes in the twentieth century and locates along the two largest cities of Myanmar, constituting a major seismic hazard. The rupture, constrained by finite-fault inversion of teleseismic body waves, backprojections of short-period *P* waves, and informed by initial Interferometric Synthetic Aperture Radar imagery of surface deformation has large slip of up to 7 m extending ~85 km north of the epicenter near Mandalay, with patchy slip of 1–6 m distributed along ~395 km to the south, with about 2 m near the capital Nay Pyi Taw. Rupture expanded at a supershear velocity of 5–6 km/s southward, during the ~80 s rupture duration. Long-period point-source moment tensors indicate eastward dip of 48.5°–60°, and such dip is required to match the teleseismic *P*-wave first motions for the early large slip in the northern part of the rupture. Dip likely steepens along strike to the south, although resolving that will require detailed analysis of surface deformation. Southward directivity associated with the finiteness and supershear rupture velocity contributed to remote distant shaking damage in Thailand.

Cite this article as Ye, L., T. Lay, and H. Kanamori (2025). The 28 March 2025 M_w 7.8 Myanmar Earthquake: Preliminary Analysis of an ~480 km Long Intermittent Supershear Rupture, *The Seismic Record*. **5**(**3**), 260–269, doi: 10.1785/0320250021.

Supplemental Material

Introduction

The tectonics of Myanmar involve collision of the Indian and Eurasia plates near the Eastern Himalayan syntaxis, southward escape tectonics of the Sunda plate, and capture of the fore-arc sliver Myanmar microplate (Fig. 1a; e.g., Le Dain *et al.*, 1984; Holt *et al.*, 1991; Wang *et al.*, 2013). Oblique relative motion between the Indian and Sunda plates is partitioned into thrusting along the northern Sunda (Arakan) trench and right-lateral strike-slip faulting along the Sagaing fault to the east, extending 1200 km from northern Myanmar to the ridge-transform fault system in the Andaman Sea (e.g., Xiong *et al.*, 2017; Mon *et al.*, 2020; Lindsey *et al.*, 2023). An eastward-dipping Wadati–Benioff zone extends from the Arakan trench to beneath the Indo-Myanmar range in western Myanmar, with seismicity down to ~160 km depth just west of the Sagaing fault (Fadil *et al.*, 2023; Mon *et al.*, 2023). A great (M > 8) earthquake in 1762 ruptured the shallow megathrust in the last major event near the trench (Wang *et al.*, 2013; Mondal *et al.*, 2018) and western Myanmar is undergoing deformation that suggests strong plate boundary coupling (Lindsey *et al.*, 2023).

The Sagaing fault is undergoing 20 ± 4 mm/yr right-lateral offset (Mallick *et al.*, 2019; Tin *et al.*, 2022), more than half of the relative motion between the Indian and Sunda plates (Tun and Watkinson, 2017). This fault extends along a very straight portion adjacent to the two most populated cities of Myanmar:

1. Department of Earth and Space Sciences, Southern University of Science and Technology, Shenzhen, China, https://orcid.org/0000-0001-9689-4149 (LY); 2. Department of Earth and Planetary Sciences, University of California Santa Cruz, Santa Cruz, California, U.S.A., https://orcid.org/0000-0003-2360-4213 (TL); 3. Seismological Laboratory, California Institute of Technology, Pasadena, California, U.S.A., https://orcid.org/0000-0001-8219-9428 (HK)

*Corresponding author: yell@sustech.edu.cn

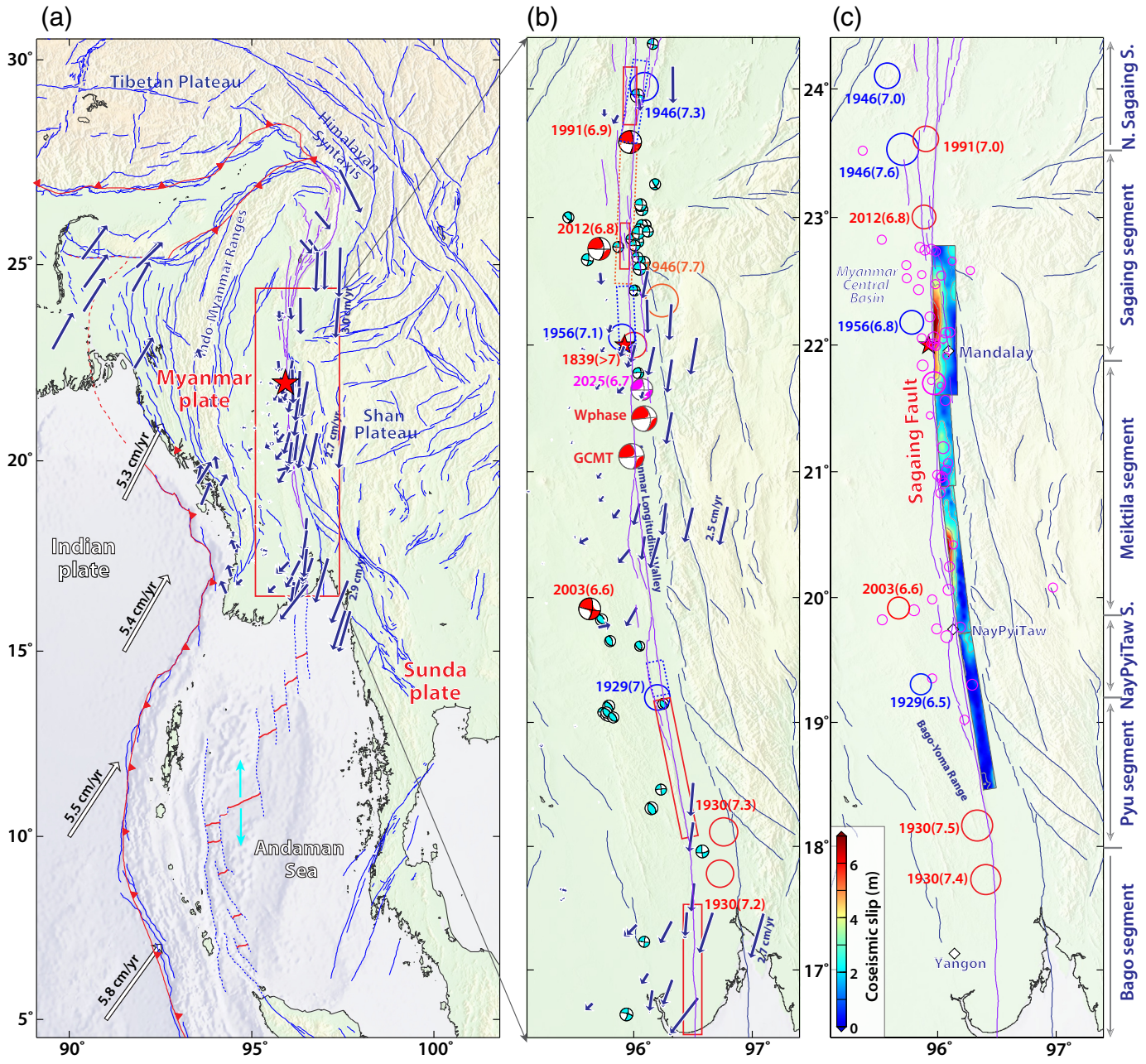

Figure 1. (a) Regional map of the topography and tectonic structures in the Indian plate, Sunda plate, and Myanmar plate region south of the eastern Himalayan syntaxis. Blue and white vectors indicate plate motions relative to the Myanmar plate from Lindsey *et al.* (2023) and the GEODVEL model (Argus *et al.*, 2010), respectively. The Myanmar plate (also called the Burma microplate) is a partially captured sliver of the Sunda plate that undergoes some internal deformation in western Myanmar and extends south along the ridge and fracture zone system in the Andaman Sea and connects to the Sumatran fault that runs along central Sumatra. The red box shows the area of zoomed-in plots in panels (b) and (c) around the right-lateral Sagaing fault along the Myanmar plate-Sunda plate margin. The red star is the U.S. Geological Survey National Earthquake Information Center (USGS-NEIC) epicenter for the 2025 M_w 7.8 Myanmar earthquake. (b) Historical seismicity along the Sagaing fault with locations of large events shown by colored circles (with corresponding rectangular estimated rupture regions; locations, earthquake magnitude, and rupture extent estimates [rectangles] from Hurukawa and Maung, 2011 and Wang *et al.*, 2014). Focal mechanisms for the 2025 M_w 7.7 mainshock and M_w 6.7 aftershock, and historical moderate events ($M_w \leq 6.5$) since 1976 are from the Global Centroid Moment Tensor (Global CMT) catalog, along with our *W*-phase moment tensor solution for the 2025 M_w 7.8 mainshock. (c) The preferred rupture model for the 2025 event along the Sagaing fault from this study is shown along with epicenters of prior large events and 1.5 months aftershocks (purple circles) from the USGS-NEIC catalog.

Mandalay and the capital Nay Pyi Taw. The northern portion of the Sagaing fault appears to have an eastward dip from the surface to 20 km depth based on fairly precise earthquake locations (Yang *et al.*, 2024). The Sagaing fault has been very active (Fig. 1b), especially in the northern portion, with six major ($M \geq 7$) ruptures in the twentieth century (e.g., Hurukawa and Maung, 2011; Fadil *et al.*, 2023). Although locations and rupture extents of older events are imprecise, a pair of M 7.4 and 7.5 events in 1930 (Tsutsumi and Sato, 2009) struck the southern Sagaing at latitudes from 17° to 18° N, whereas M 7.3 and M 7.7 events in 1946 and an M 7.1 event in 1956 struck at latitudes of 22°–24° N (Fig. 1b). Consideration of these ruptures led Hurukawa and Maung (2011) to identify a seismic gap from 19° to 21.5° N, extending between the two major cities.

The Sagaing fault seismic gap ruptured in an M_w 7.7–7.8 earthquake on 28 March 2025. The U.S. Geological Survey National Earthquake Information Center (USGS-NEIC) epicentral location is (21.996° N, 95.926° E) at 06:20:52.684 UTC with a depth of 10.0 km. The USGS-NEIC reports a W-phase point-source moment tensor with seismic moment 4.634×10^{20} N · m (M_{ww} 7.71, based on the W-phase solution), with best-double-couple solution of strike 1°, dip 82°, and rake −174°, at a centroid depth of 40.5 km. The 82° eastward dipping geometry was adopted in a series of finite-source inversion using seismic and geodetic (Interferometric Synthetic Aperture Radar [InSAR]) data, but it is important that the Global Centroid Moment Tensor (Global CMT) solution (centroid time 06:21:23.5 UTC; seismic moment 5.13×10^{20} N · m [M_w 7.7]) has a much shallower centroid depth of 20.1 km and the best double couple has strike 353°, dip 60°, and rake 175°, suggesting that the dip estimate depends on estimated source depth. Given the large surface deformation observed, a centroid depth of 40.5 km is unlikely. An M_w 6.7 aftershock struck about 11 min after and 59 km south of the mainshock, for which the Global CMT solution has a centroid depth of 19.1 km and a dip of 73°, suggesting southward steepening of the fault dip. Here, we re-evaluate the point-source solution from W-phase inversion and incorporate improved geometry constraints into a first-order finite-fault model (Fig. 1c) inverted from global seismic body waves that is constrained using teleseismic short-period network backprojections and initial InSAR surface deformation observations.

Point-Source Inversion

The 2025 rupture produced strong surface deformation documented in media coverage and preliminary InSAR measurements, so the centroid depth is probably located in the shallow crust, not at 40.5 km from the USGS-NEIC W-phase solution, and this affects the point-source inversion. We thus performed new W-phase inversions (Kanamori and Rivera, 2008) to better constrain the appropriate moment tensor. Using the preliminary reference Earth model (PREM; Dziewonski and Anderson, 1981) for 36 stations with 90 channels in the frequency passband of 0.002–0.01 Hz and searching over centroid depth gave a preferred depth of 25.5 km with a best double couple having strike 354.6°, dip 51.4°, and rake −179.4°. This solution has a much lower dip than that for a depth of 40.5 km, indicating a strong trade-off between dip and centroid depth for this event. This explains why the use of the solution with a steep dip by the NEIC provides very poor waveform fits to teleseismic P and SH waves at many azimuths, violating clear first motions (the USGS-NEIC slip model predictions are downloadable through the page link). Cai *et al.* (2025) also note that this discrepancy of the USGS-NEIC W-phase solution relative to other global point-source solutions. Although a steeply dipping strike-slip fault seems plausible, the seismic data for at least the early portion of the rupture unambiguously require a shallower dip, as indicated by our initial W-phase inversion. We then used the same data set and a different database of Green's functions (JAPREM: A 33 km thick crust is used for distances less than 30° whereas PREM is used for larger distances) for a W-phase inversion optimizing centroid depth, duration, and location of the point source. This gives a solution with a centroid depth of 17.5 km with a best-double-couple solution having strike 354°, dip 48.5°, and rake −179.7°, reinforcing the need for shallower dip. Expanding the data set to 247 channels and using JAPREM gave a final W-phase solution with strike 0.2°, dip 43.8°, rake 177.4°, seismic moment of 5.65×10^{20} N · m (M_w 7.77), a half duration of 29.5 s, and centroid location (21.52° N, 96.194° E; Fig. 1b). This solution has a moderately large non-double-couple component. A bootstrap analysis indicates estimates for strike of 353.9° ± 0.8°, dip 54.6° ± 2.5°, and rake 172.2° ± 1.6°, with minor trade-off between strike and dip (Fig. S1, available in the supplemental material to this article). A dip close to 50° is strongly favored, and we will use 48.5° for the northern subfault in our finite-fault solution below, recognizing that there is ±5° uncertainty, but it clearly must be much lower than 82° as assumed for the whole fault in the USGS-NEIC solution. Such a shallow dip for a significant portion of a large strike-slip rupture has been observed in the South Scotia Sea (Ye *et al.*, 2014).

Backprojection Images

Backprojection of short-period P waves from regional and global networks often provides useful information about the

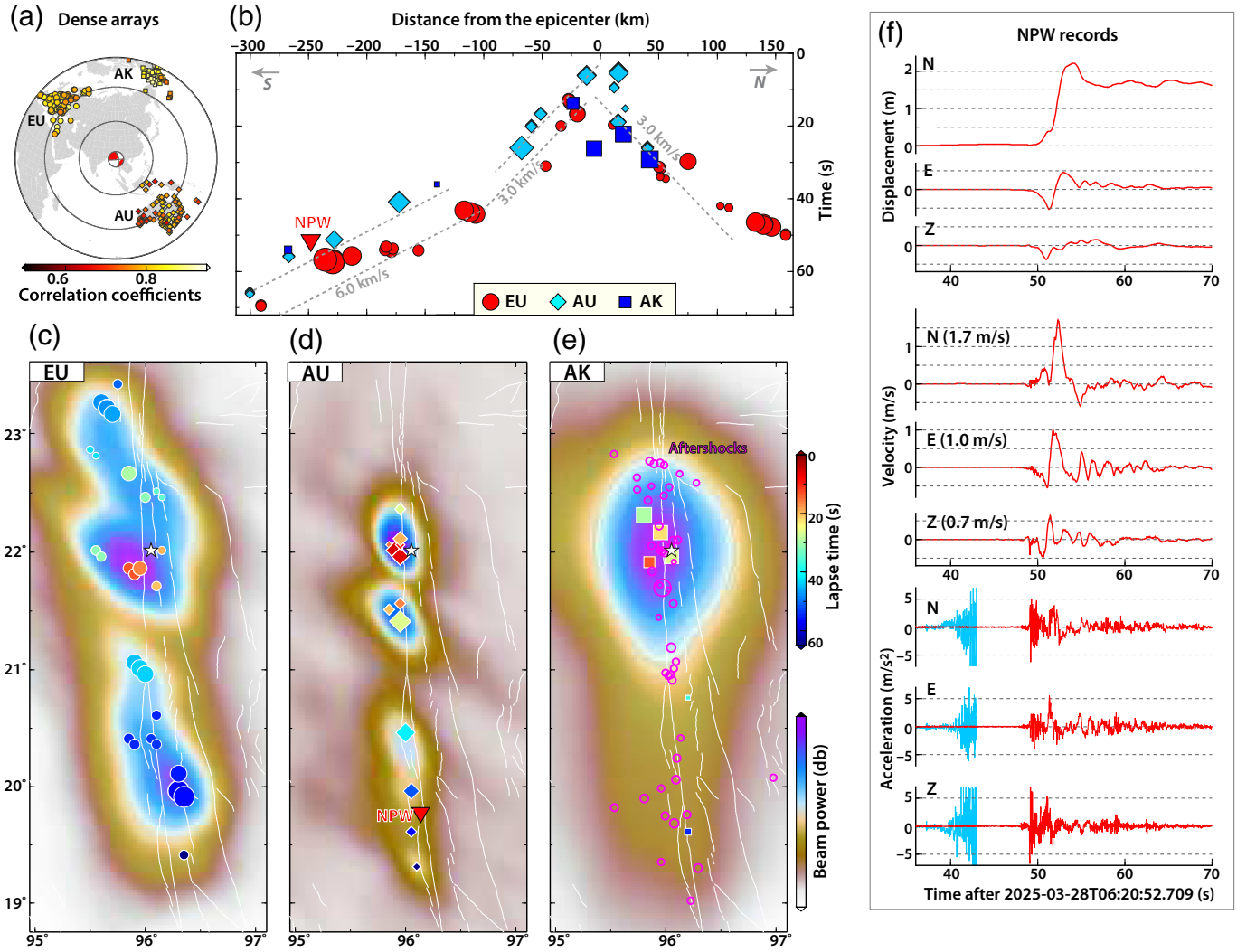

kinematics and heterogeneity of large ruptures with few a priori constraints on the source geometry and extent (e.g., Kiser and Ishii, 2017), and this has played a particularly important role in recognizing supershear rupture intervals of numerous large strike-slip earthquakes. The 2025 Myanmar earthquake source is favorably located for backprojection analysis using large regional networks of broadband seismic stations around Europe, Alaska, and Australia (Fig. 2a). Raw broadband vertical-component *P*-wave recordings were aligned by cross correlations for each network and were then band-pass filtered (0.5–2.0 Hz) to be backprojected to grids around the Sagaing fault at the depth of 10.0 km. Bursts of coherent short-period beam power detected in the images for each network are plotted as a function of distance and time from the hypocenter (Fig. 2b), and the corresponding overall backprojection spatial patterns are shown in Figure 2c–e. All three network images

Figure 2. (a) Locations of teleseismic networks of vertical-component broadband stations around Europe (EU), Australia (AU), and Alaska (AK). (b) The time–distance from epicenter of short-period energy bursts (0.5–2.0 Hz) in the backprojections for the three arrays (indicated by different symbols). The red triangle indicates the arrival of the displacement pulse at the strong-motion station NPW (51.5 s at 248 km from the epicenter). Moveout curves for rupture velocities of 3.0 and 6.0 km/s are indicated. Supershear rupture appears to occur after ~75 km to the south. (c–e) Beam power for backprojections from the EU, AU, and AK networks, respectively. Symbol colors indicate time after event onset at the locations of localized energy bursts within a time window of 5 s. The white star indicates the epicenter. White curves are fault traces from the Active Faults of Eurasia Database (AFEAD; Zelenin *et al.* 2022). Location of NPW is indicated in panel (d). Aftershocks from the USGS-NEIC from 28 March to 12 May are indicated by magenta circles in panel (e). (f) Three-component ground motions at station NPW, which is ~5 km west of the Sagaing fault near the capital Nay Pyi Taw. Note the strong northward static displacement of ~1.5 m initially beginning at about 51.5 s. In the acceleration plots, the cyan signal is the ground acceleration multiplied by 600, revealing the arrival of *P* energy ~12 s before strong signals associated with the rupture front arrival.

indicate an asymmetric bilateral rupture, with much greater extent to the south along the trend of the Sagaing fault and the early aftershock distribution (Fig. 2e). The backprojection image details differ between the three networks: a typical consequence of influences of rupture directivity, azimuthal difference in Green's functions due to fault orientation, and variable network imaging resolution relative to the source geometry. Constraining the backprojections to the fault location results in a very similar pattern of rupture expansion. We do not perform joint inversion of the network data due to these differences, which raise issues of short-period signal coherence, and have not applied any corrections for long-strike variations in data alignments, which may improve images in future work.

The short-period coherent energy burst locations have some baseline shifts between networks (Fig. 2b), reflecting the waveform differences at different azimuths, but display consistent trends in apparent rupture velocity connecting the bursts in both directions along the fault strike, assuming the short-period radiation tends to track the rupture front. The northward rupture appears to extend more than 75 km from the hypocenter with a rupture velocity of ~3.0 km/s, noting that backprojection images often spread signal excessively along strike in the direction of the imaging network (here, toward the European network EU). The southward rupture appears to extend ~75 km southward with a similar inferred rupture velocity of 3.0 km/s, followed by a clear increase in rupture speed for the next 200 km at a supershear rupture speed of ~6 km/s. There is at least ±1 km/s uncertainty in these estimates. All three networks indicate intermittent supershear rupture speed in the southern part of the rupture. Bilateral rupture is also noted by Inoue *et al.* (2025).

An important record for this earthquake is that from a near-fault strong-motion station NPW, located ~5 km west of the Sagaing fault and ~248 km from the epicenter (Fig. 2d,f). NPW is near the capital city Nay Pyi Taw, which experienced significant shaking damage. The accelerations show very weak initial *P*-wave arrivals about 36 s after the origin time (predicted *Pn*-arrival time is 39.25 s), with much stronger motions commencing ~12 s later. Strong linearly increasing northward displacement at 51.5 s after the origin indicates the onset of static deformation, which is ultimately ~1.5 m to the north. From 48 to 51.5 s, there is a complex displacement motion likely involving compression and shear energy preceding the arriving rupture front. This record will undoubtedly be extensively modeled in the future, but for our purposes, the kinematics and the distinct stepwise displacement are the strong evidence that the fault slip motion occurred near NPW (248 km) at about 51.5 s and indicate an average rupture velocity minimum of 248 km/51.5 s = 4.8 km/s. As it will take ~2 s for displacement to elastically spread through the crust across the 5 km distance from the fault, the average rupture velocity may be ~5.0 km/s. If the southward rupture expands at 3.0 km/s for the first 75 km, the average rupture velocity the rest of the way to NPW can be estimated as ~7.0 km/s, basically compatible with the backprojection images (see point NPW in Fig. 2b). Although complete dynamic waveform modeling may lead to minor changes of these numbers, the clear implication is that the southern rupture was substantially supershear. The slip pulse duration at NPW involves ~1.5 s duration with 1.5 m static offset, with particle velocity of ~1.0 m/s. There is some overshoot of the northward displacement, which is likely due to superimposed transient Love-wave tangential motion. Total offset on the fault would be double the displacement on the west side recorded by NPW, so ~3.0 m of total slip occurred near the capital.

Finite-Fault Inversion

The 2025 Myanmar earthquake produced global recordings of seismic waves that can reveal more details of the slip distribution. Local recordings are limited, in part due to the political instability in the country, but a couple of strong-motion stations recorded onscale signals at larger distances than NPW (Figs. S2, S3). Regional stations are largely distributed eastward from the source and will feature prominently in future surface-wave analyses, but for a preliminary finite-fault model, we will use teleseismic broadband *P* and *SH* recordings to constrain basic features of the faulting. We obtained 64 broadband *P*-wave ground displacement recordings and 35 broadband *SH*-wave ground velocity recordings from azimuthally well-distributed global network stations downloaded from the Incorporated Research Institutions for Seismology Data Management Center (IRIS-DMC). We specify a fault model representing the Sagaing fault and perform a linear least-squares kinematic inversion for slip on the fault (Kikuchi and Kanamori, 1991; Ye *et al.*, 2016). A regional 1D crustal velocity structure (Shiddiqi *et al.*, 2019) is assumed for the source region.

In specifying the fault model, we adopt a four-planar segment representation with strike and dip varying along the model (Fig. 3b) over a total length of 480 km. The dip of the 130 km long northern segment (F1) is 48.5°, representative of the dip for the point-source moment tensors, then the dip increases to 60° in the adjacent 80 km long segment (F2) to

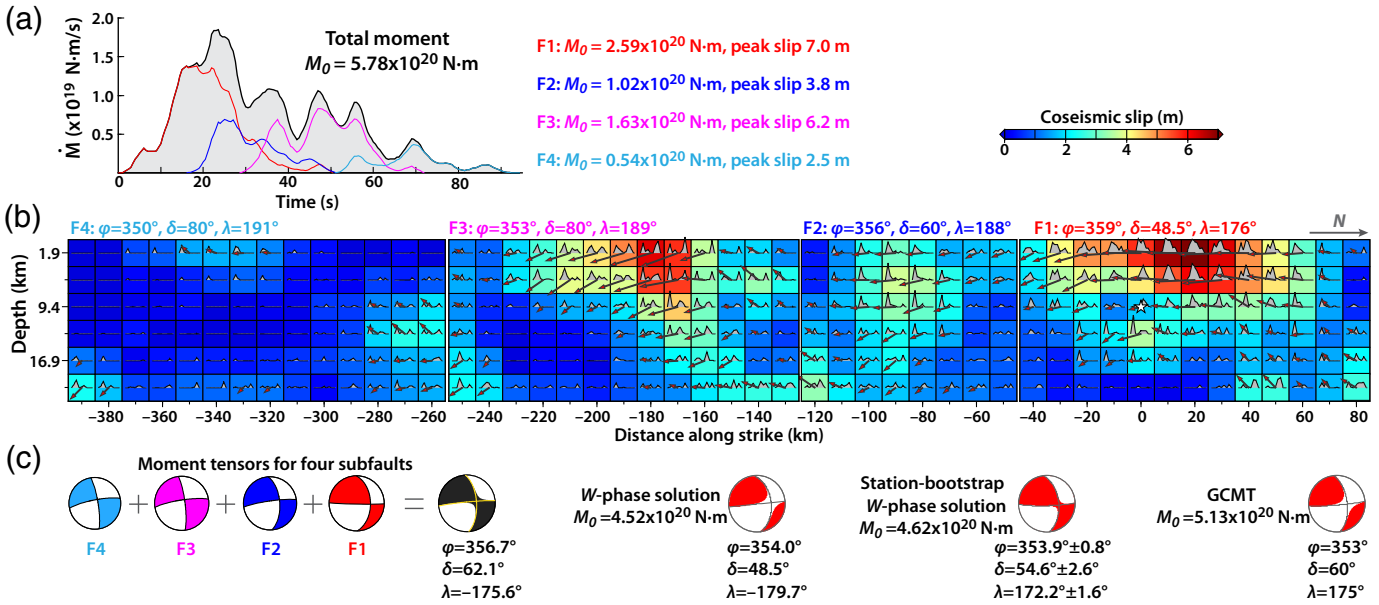

Figure 3. Source model for the 2025 Myanmar earthquake inverted from teleseismic *P* and *SH* waves using least-squares kinematic inversion. (a) Moment rate function for the overall source (gray-shaded region) with contributions from each of the four subfaults along strike indicated by colored curves with parameters given on the right. (b) Distribution of slip in the model, with faulting orientation of each segment shown above the segments. The colors indicate the magnitude of slip in each subfault, with the vectors indicating the sliding motion of the hanging wall (eastern side) relative to the foot wall (western side), with length proportional to slip. The subfault source time functions are shown within each subfault with gray polygons with common scale. (c) Comparison of the composite solution for the four subfaults in the model, the favored *W*-phase moment tensor, the solution with uncertainties by the station bootstrap analysis (1000 resamples, see Fig. S1), and the Global CMT solution.

the south and then to 80° in the southern two segments (F3 and F4) which extend 130 and 140 km, respectively. The southward increase in dip is not resolved by our data, but is motivated by the very straight southern fault outcrop and the transition to supershear rupture, which favors a simple fault geometry. InSAR images processed for pixel offsets by the USGS-NEIC show broader, somewhat asymmetric regions of deformation across the fault in the north and narrower more symmetric distributions in the south of the rupture, compatible with our overall model geometry. The strike rotates counterclockwise by a total of ∼10° over the four segments, tracking the fault outcrop seen in Figure 1, and extending over the full length of InSAR-detected surface offsets (from 18.5° to 22.8° N, see Fig. 1c). The rupture velocity on the northern segment is allowed to be as high as 3.0 km/s, whereas it is as high as 6.0 km/s on the three southern segments, guided by the back-projection results in Figure 2. The fault model parameterizes the subfault source time functions with seven 3 s rise time triangles with corresponding time offsets, allowing up to 24 s subfault rupture durations that accommodate both average and interval rupture velocity variations. Future detailed analysis of the surface deformation will refine the geometry, but we believe this is a reasonable fault system representation for modeling teleseismic data.

The inversion result for this model is shown in Figure 3. The residual normalized waveform power is ∼24.8%, which is quite good for a long complex strike-slip rupture. Most slip is concentrated in the upper 10 km with patchy deeper slip not well resolved. Peak slip on the northern subfault F1, with shallowest dip, is 7.0 m with shallow slip exceeding 4 m along an 80 km extent. The seismic moment of segment F1 is almost half of the total, 5.78×10^{20} N · m (M_w 7.8), which is comparable to the combined seismic moment of segments F2 and F3, with peak slip of 3.8 and 6.2 m, respectively. Minor, less well-resolved slip is located on F4 with the source duration extending to at least 80 s, possibly with minor radiation to 90 s. The moment rate function and along strike-slip distribution is generally similar to the USGS-NEIC model, which directly inverts the teleseismic and InSAR observations. However, the *P* and *SH* waveform fits for our model (Fig. 4) are significantly better than those for the USGS-NEIC model posted at the time this article is being written, fitting the polarities and amplitudes of many stations that are totally misfit by the latter model. The moment tensors for each subfault and the composite solution for the

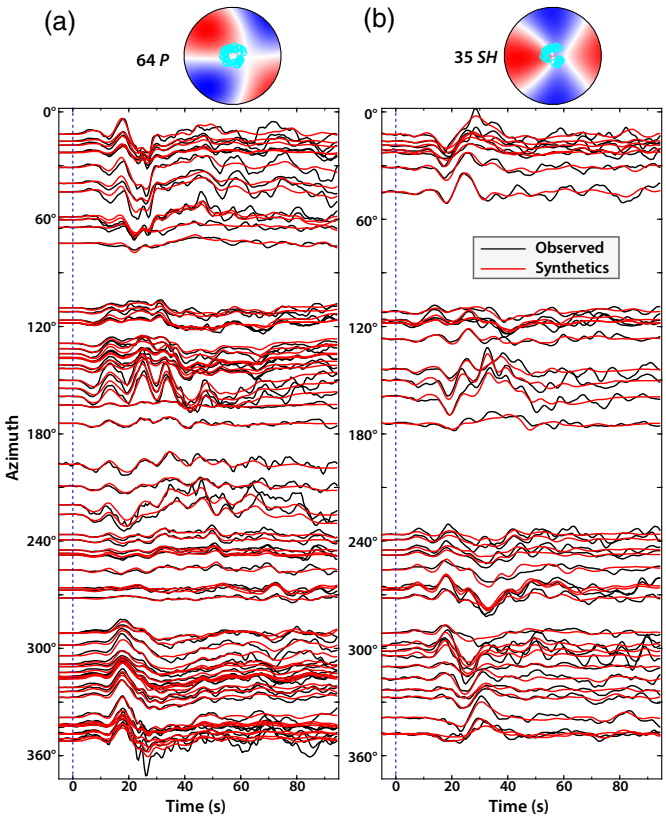

Figure 4. Comparison of observed (black curves) and preferred model predicted (red curves). (a) Teleseismic *P* ground displacements and (b) teleseismic *SH*-wave ground velocities. The traces are shown with true relative amplitudes for *P* and for *SH* separately normalized. The *P* and *SH* radiation mechanisms shown at the top indicate the distribution of takeoff and azimuth angles sampled by the data relative to the radiation nodes.

total rupture in our model are consistent with our *W*-phase solution and the bootstrap estimates on the strike, dip, and rake (Fig. 3c); therefore, this model is consistent with teleseismic body waves and very long period seismic energy. Our own preliminary joint models of teleseismic and InSAR observations are quite similar to the model presented here, so the main important improvement relative to the USGS-NEIC model comes from using a fault orientation with shallower dip in the north consistent with the point-source moment tensors for sources with reasonable centroid depth.

Discussion and Conclusion

The ~480 km long rupture of the 2025 Myanmar earthquake is exceptionally long for an M_w 7.8 strike-slip rupture, comparable to the >400 km long 1906 San Francisco (Wald *et al.*, 1993), 2001 Kunlun (Bouchon and Vallée, 2003), and 2017 Komandorsky (Lay *et al.*, 2017) earthquakes, and longer than the ~380 km long rupture of the 2013 South Scotia earthquake (Ye *et al.*, 2014), the ~350 km long rupture of the 2023 East Anatolian fault (Liu *et al.*, 2023), and the ~290 km long rupture of the 2002 Denali earthquake (Haeussler *et al.*, 2004). In 1839, the same stretch of the Sagaing fault ruptured in an event (Fig. 1b) with estimated magnitude of up to 7.9, but the 2025 rupture length extended further along strike than the seismic gap region identified by Hurukawa and Maung (2011), overlapping regions that may have ruptured in a 1930 event to the south and a 1956 event to the north (Fig. 1b). The weak patchy slip in the southernmost subfault (F4 in our model) does suggest the possibility that slip may have been complementary to slip in the 1930 event in the south; the exact slip distributions in 1930 and 1956 are not known.

Figure 5a shows the far-field source spectrum for the 2025 Myanmar earthquake, compared to the reference spectrum for a point-source event with the same seismic moment and a 3 MPa stress factor (e.g., Ye *et al.*, 2016). The 2025 spectrum is estimated from the moment rate function in Figure 3a for frequencies below 0.05 Hz and from a stack of teleseismic *P*-wave displacement spectra observations corrected for propagation and radiation pattern effects for frequencies from 0.05 to 2.0 Hz, following the procedure in Ye *et al.* (2016). The radiated energy E_R for the event is estimated to be $E_R = 1.05 \times 10^{16}$ J, slightly higher than the broadband radiated energy estimate of 6.1×10^{15} J in the passband of 0.5–70 s given by the IRIS-DMC (see Data and Resources). The moment scaled radiated energy is 2.05×10^{-5}, which is twice the value for global interplate thrust events found by Ye *et al.* (2016).

To compare the seismic-wave radiation from the 2025 M_w 7.8 Myanmar earthquake with that from earlier large events on the Sagaing fault and with global observations, we measured m_B from broadband *P*-wave ground displacement seismograms from the global digital network following the procedure of Kanamori and Ross (2018), along with 20 s period M_s values (Fig. 5b). The 2025 M_w 7.8 Myanmar event has m_B 7.2 and M_s 7.8. The m_B estimate is similar to those for Sagaing ruptures in 1912 (7.3), 1931 (7.3), and 1946 (7.4), so there is some consistency in the shorter period body-wave radiation from these events on the same fault, with slightly lower values than the overall average for the global population including events before and after 1990. The greater severity of the damage for the 2025 event likely reflects both the increase of the population in the two large cities along the rupture and the unusual long slip zone with supershear velocity.

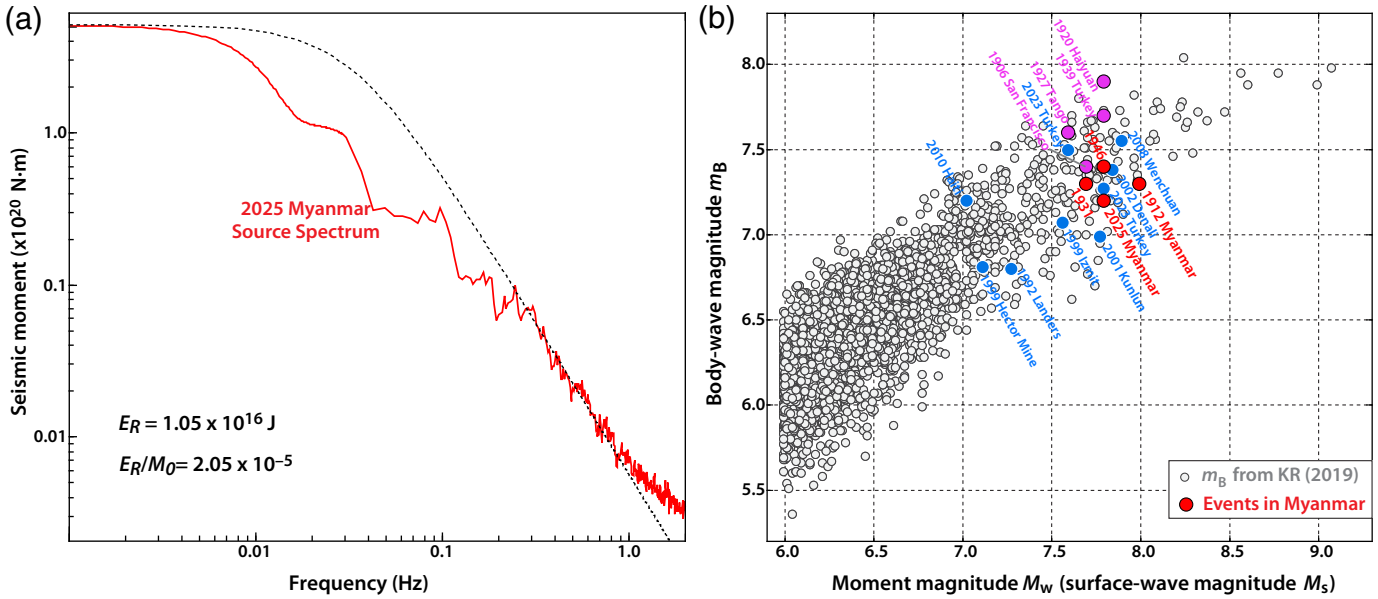

Figure 5. (a) Far-field source spectrum for the 2025 Myanmar earthquake estimated from the moment rate function from finite-fault inversion in Figure 3a for frequencies <0.05 Hz and from stacking radiation-pattern corrected broadband teleseismic *P*-wave displacement spectra for frequencies of 0.05–2.0 Hz (red curve) compared to an ω^{-2} reference source spectrum with the same seismic moment and a stress factor of 3 MPa. (b) Long-period body-wave magnitudes, m_B, for global large earthquakes with $M_W(M_S) \geq 6.0$. Red points indicate large events along the Sagaing fault in Myanmar, including the 2025 event. Points for other large strike-slip events are indicated in blue (events after 1990) and magenta (events prior to 1990) with other events from Kanamori and Ross (2018).

The 2025 M_w 7.8 Myanmar earthquake adds to the number of large strike-slip events that have at least portions of their ruptures experience supershear rupture. The southward directed supershear segment rupture propagated with a velocity of 5–6 km/s over several hundred kilometers distance, with rather compelling evidence from the southward fault length and InSAR measures of surface displacement and the rupture duration (~380 km in ~80 s implies ~5 km/s) from the backprojections at multiple teleseismic networks (~6 km/s along ~200 km of the southern rupture), and from the timing of static deformation at station NPW (>4.8 km/s). Additional constraints should be provided by future analysis of broadband surface waves to the southeast where a Mach cone is predicted with little dispersion of surface wave pulses. Whether supershear initiated at the surface or in transits of sedimentary basins and whether *P*-wave triggering was involved will all require further analysis. The strong concentration of damage in Bangkok documented in the media for this event is a testimonial to the potentially severe effects of rupture directivity enhanced by occurrence of supershear rupture.

Data and Resources

Seismic recordings from global seismic stations we used were downloaded from the National Science Foundation (NSF) Seismological Facility for the Advancement of Geoscience (SAGE) Incorporated Research Institutions for Seismology Data Management Center (IRIS-DMC, http://ds.iris.edu/ds/nodes/dmc/). Strong-motion data were downloaded from the Center for Engineering Strong-Motion Data (CESMD; https://www.strongmotioncenter.org/). Earthquake source mechanisms are from the Global Centroid Moment Tensor (Global CMT) project (Ekström *et al.*, 2012). Earthquake information is based on the catalogs of the National Earthquake Information Center (NEIC) at the U.S. Geological Survey (USGS, https://earthquake.usgs.gov/earthquakes/eventpage/us7000pn9s/executive). The earthquake energy product query is available at https://ds.iris.edu/spud/eqenergy. All websites were last accessed in April 2024. Additional tables and figures are included in the supplemental material to this article.

Declaration of Competing Interests

The authors acknowledge that there are no conflicts of interest recorded.

Acknowledgments

The authors thank Shiqing Xu, Zhenxing Yao, Xiaofei Chen, and Xiaohua Xu for helpful discussions, Editor-in-Chief

Keith Koper and an anonymous reviewer for their thoughtful comments and suggestions, which helped improve the article. The work was supported in part by National Natural Science Foundation of China 42474077 (L. Y.) and National Science Foundation Grant EAR1802364 (T. L.).

References

Argus, D. F., R. G. Gordon, M. B. Heflin, C. Ma, R. J. Eanes, P. Willis, W. R. Peltier, and S. E. Owen (2010). The angular velocities of the plates and the velocity of Earth's centre from space geodesy, *Geophys. J. Int.* **180,** no. 3, 913–960, doi: 10.1111/j.1365-246X.2009.04463.x.

Bouchon, M., and M. Vallée (2003). Observation of long supershear rupture during the magnitude 8.1 Kunlunshan earthquake, *Science* **301,** 824–826, doi: 10.1126/science.1086832.

Cai, J., N. Xi, G. Han, W. Deng, and L. Sun (2025). Rapid report of the March 28, 2025 Mw 7.9 Myanmar earthquake, *Earthq. Res. Adv.* doi: 10.1016/j.eqrea.2025.100396.

Dziewonski, A. M., and D. L. Anderson (1981). Preliminary reference Earth model, *Phys. Earth Planet. In.* **25,** no. 4, 297–356.

Ekström, G., M. Nettles, and A. M. Dziewoński (2012). The global CMT project 2004–2010: Centroid-moment tensors for 13,017 earthquakes, *Phys. Earth Planet. In.* **200,** 1–9.

Fadil, W., S. Wei, K. Bradley, Y. Wang, Y. He, E. Sandvol, B.-S. Huang, J. Hubbard, M. Thant, and Y. M. M. Htwe (2023). Active faults revealed and new constraints on their seismogenic depth from a high-resolution regional focal mechanism catalog in Myanmar (2016-2021), *Bull. Seismol. Soc. Am.* **113,** 613–635, doi: 10.1785/0120220195.

Haeussler, P. J., D. P. Schwartz, T. E. Dawson, H. D. Stenner, J. J. Lienkaemper, B. Sherrod, F. R. Cinti, P. Montone, P. A. Craw, A. J. Crone, *et al.* (2004). Surface rupture and slip distribution of the Denali and Totschunda Faults in the 3 November 2002 M 7.9 earthquake, Alaska, *Bull. Seismol. Soc. Am.* **94,** S23–S52, doi: 10.1785/0120040626.

Holt, W. E., F. N. James, T. C. Wallace, and A. J. Haines (1991). The active tectonics of the eastern Himalayan syntaxis and surrounding regions, *J. Geophys. Res.* **96,** 14,595–14,632, doi: 10.1029/91JB01021.

Hurukawa, N., and P. M. Maung (2011). Two seismic gaps on the Sagaing Fault, Myanmar, derived from relocation of historical earthquakes since 1918, *Geophys. Res. Lett.* **38**, L01310, doi: 10.1029/2010GL046099.

Inoue, N., R. Yamaguchi, Y. Yaghi, R. Okuwaki, B. Enescu, and T. Tadapansawut (2025). A multiple asymmetric bilateral rupture sequence derived from the peculiar teleseismic P-waves of the 2025 Mandalay, Myanmar earthquake, *Seismica* **4,** 1–8, doi: 10.26443/seismica.v4i1.1691.

Kanamori, H., and L. Rivera (2008). Source inversion of Wphase: Speeding up seismic tsunami warning, *Geophys. J. Int.* **175,** 222–238, doi: 10.1111/j.1365-246X.2008.03887.x.

Kanamori, H., and Z. E. Ross (2018). Reviving m_B, *Geophys. J. Int.* **216,** 1798–1816, doi: 10.1093/gji/ggy510.

Kikuchi, M., and H. Kanamori (1991). Inversion of complex body waves—III, *Bull Seismol. Soc. Am.* **81,** 2335–2350, doi: 10.1785/bssa0810062335.

Kiser, E., and M. Ishii (2017). Back-projection imaging of earthquakes, *Ann. Rev. Earth Planet. Sci.* **45,** 271–299, doi: 10.1146/annurev-earth-063016-015801.

Lay, T., L. Ye, Y. Bai, K. F. Cheung, H. Kanamori, J. Freymueller, G. M. Steblov, and M. G. Kogan (2017). Rupture along 400 km of the Bering fracture zone in the Komandorsky Islands earthquake (M_W 7.8) of 17 July 2017, *Geophys. Res. Lett.* **44,** 12,161–12,169, doi: 10.1002/2017GL076148.

Le Dain, A. Y., P. Tapponnier, and P. Molnar (1984). Active faulting and tectonics of Burma and surrounding regions, *J. Geophys. Res.* **89,** 453–472, doi: 10.1029/JB089iB01p00453.

Lindsey, E. O., Y. Wang, L. T. Aung, J.-H. Chong, Q. Qiu, R. Mallick, L. Feng, P. S. Aung, T. Z. H. Tin, S. M. Min, *et al.* (2023). Active subduction and strain partitioning in western Myanmar revealed by a dense survey of GNSS network, *Earth Planet. Sci. Lett.* **622,** 118384, doi: 10.1016/j.epsl.2023.118384.

Liu, C., T. Lay, R. Wang, T. Taymaz, Z. Xie, X. Xiong, T. S. Irmak, M. Kahraman, and C. Erman (2023). Complex multi-fault rupture and triggering during the 2023 earthquake doublet in southeastern Türkiye, *Nat. Commun.* **14,** 5564, doi: 10.1038/s41467-023-41404-5.

Mallick, R., E. O. Lindsey, L. Feng, J. Hubbard, P. Banerjee, and E. M. Hill (2019). Active convergence of the India-Burma-Sunda plates revealed by a new continuous GPS network, *J. Geophys. Res.* **124,** 3155–3171, doi: 10.1029/2018JB016480.

Mon, C. T., X. Gong, Y. Wen, M. Jiang, Q.-F. Chen, M. Zhang, G. Hou, M. Thant, K. Sein, and Y. He (2020). Insight into major active faults in Central Myanmar and the related geodynamic sources, *Geophys. Res. Lett.* **47,** e2019GL086236, doi: 10.1029/2019GL086236.

Mon, C. T., S. Yang, C. Ren, Y. He, M. Thant, and K. Sein (2023). New insight into the subducted Indian plate beneath central Myanmar based on seismic activity and focal mechanisms analysis, *Seismol. Res. Lett.* **94,** 2337–2347, doi: 10.1785/0220220381.

Mondal, D. R., C. M. McHugh, R. A. Mortlock, M. S. Steckler, S. Mustaque, and S. H. Akhter (2018). Microatolls document the 1762 and prior earthquakes along the southeast coast of Bangladesh, *Tectonophysics* **745,** 196–213, doi: 10.1016/j.tecto.2018.07.020.

Shiddiqi, H. A., P. P. Tun, and L. Ottemöller (2019). Minimum 1D velocity model and local magnitude scale for Myanmar, *Seismol. Res. Lett.* **90,** 1923–1936, doi: 10.1785/0220190065.

Tin, T. Z. H., T. Nishimura, M. Hashimoto, E. O. Lindsey, L. T. Aung, S. M. Min, and M. Thant (2022). Present-day crustal deformation and slip rate along the southern Sagaing fault in Myanmar by GNSS observation, *J. Asian Earth Sci.* **228,** doi: 10.1016/j.jseaes.2022.105125.

Tsutsumi, H., and T. Sato (2009). Tectonic geomorphology of the southernmost Sagaing fault and surface rupture associated with the May 1930 Pegu (Bago) earthquake, Myanmar, *Bull. Seismol. Soc. Am.* **99,** 2155–2168.

Tun, S. T., and I. M. Watkinson (2017). Chapter 19 The Sagaing Fault, Myanmar, in *Myanmar: Geology, Resources and Tectonics*, A. J. Barber, K. Zaw, and M. J. Crow (Editors), Vol. 48, Geological Society, London, United Kingdom, 413–441, doi: 10.1144/M48.19.

Wald, D. J., H. Kanamori, D. V. Helmberger, and T. H. Heaton (1993). Source study of the 1906 San Francisco earthquake, *Bull. Seismol. Soc. Am.* **83,** no. 4, 981–1019, doi: 10.1785/BSSA0830040981.

Wang, Y., J. B. H. Shyu, K. Sieh, H. W. Chiang, C. C. Wang, T. Aung, Y. N. N. Lin, C. C. Shen, S. Min, O. Than, *et al.* (2013). Permanent upper plate deformation in western Myanmar during the great 1762 earthquake: Implications for neotectonic behavior of the northern Sunda megathrust, *J. Geophys. Res.* **118,** 1277–1303, doi: 10.1002/jgrb.50121.

Wang, Y., K. Sieh, S. T. Tun, K.-Y. Lai, and T. Myint (2014). Active tectonics and earthquake potential of the Myanmar region, *J. Geophys. Res.* **119,** 3767–3822, doi: 10.1002/2013JB010762.

Xiong, X., B. Shan, Y. M. Zhou, S. J. Wei, Y. D. Li, R. Wang, and Y. Zheng (2017). Coulomb stress transfer and accumulation on the Sagaing Fault, Myanmar, over the past 110 years and its implications for seismic hazard, *Geophys. Res. Lett.* **44,** 4781–4789, doi: 10.1002/2017GL072770.

Yang, S., Z. Xiao, S. Wei, Y. He, C. T. Mon, G. Hou, M. Thant, K. Sein, and M. Jiang (2024). New insights into active faults revealed by a deep-learning-based earthquake catalog in Central Myanmar, *Geophys. Res. Lett.* **51,** e2023GL105159, doi: 10.1029/2023GL105159.

Ye, L., T. Lay, H. Kanamori, and L. Rivera (2016). Rupture characteristics of major and great ($M_W \geq 7$) megathrust earthquakes from 1990 to 2015: 1. Source parameter scaling relationships, *J. Geophys. Res.* **12,** no. 2, 826–844, doi: 10.1002/2015jb012426.

Ye, L., T. Lay, K. D. Koper, R. Smalley Jr., L. Rivera, M. G. Bevis, A. F. Zakrajsekand, and F. N. Teferle (2014). Complementary slip distributions of the August 4, 2003 M_W 7.6 and November 17, 2013 M_W 7.8 South Scotia Ridge earthquakes, *Earth Planet. Sci. Lett.* **401,** 215–226, doi: 10.1016/j.epsl.2014.06.007.

Zelenin, E., D. Bachmanov, S. Garipova, V. Trifonov, and A. Kozhurin (2022). The active faults of Eurasia database (AFEAD): The ontology and design behind the continental-scale dataset, *Earth Syst. Sci. Data* **14,** no. 10, 4489–4503.

Manuscript received 22 May 2025
Published online 10 July 2025